ADVANCED HEALTHCARE MATERIALS
www.advhealthmat.de

Advancing Targeted Drug Delivery in Glioblastoma Multiforme Through Biomimetic Nanomedicine Using 3D Tumor-On-a-Chip Model

Twinkle Jina Minette Manoharan, Ting-Yun Wang, Shivani Mantri, Hanan Alarnous, Shwetal Mehta, Kuei-Chun Wang, and Mehdi Nikkhah**

The prognosis of glioblastoma multiforme (GBM) remains dismal, despite standard treatment regimens. A key challenge in treating GBM is the persistence of glioma stem cells (GSCs) within the perivascular niche (PVN) – a protective tumor microenvironment (TME) that is often associated with inadequate drug penetration. Current preclinical models do not capture complexity of the human TME, particularly the vasculature and niche-specific interactions that drive GBM progression. To overcome these limitations, an innovative 3D *ex-vivo* tumor-on-a-chip (TOC) platform is engineered to accurately replicate the structural and functional characteristics of the PVN. Using this platform, this study demonstrates that monocyte membrane-coated nanoparticles (MoNP) effectively target the abnormal tumor microvasculature, offering a promising approach to enhance drug delivery to these hard-to-reach GSCs. The results show that the therapeutic agent verteporfin, when delivered via MoNP, significantly inhibited GSC growth and invasiveness, while the free-form drug showed minimal efficacy. Comprehensive transcriptomic profiling and cytokine analysis validated the TOC model's ability to reflect authentic GSC responses and confirmed that MoNP-mediated verteporfin delivery effectively modulates key tumor-related signaling pathways. This integrated TOC-MoNP platform represents a clinically relevant tool that bridges the gap between traditional preclinical models and human disease, providing new opportunities for developing more effective GBM therapies.

1. Introduction

Glioblastoma multiforme (GBM), the most aggressive and lethal form of brain tumor in adults, presents a formidable clinical challenge.[1] Despite multimodal interventions such as maximal surgical resection, radiation, and chemotherapy, the outlook for patients remains poor, with only 5% surviving beyond 5 years after diagnosis.[2] Growing evidence implicates glioma stem cells (GSCs), as central drivers of tumor growth, invasion, and therapeutic resistance, contributing to GBM progression and recurrence.[3] Studies have demonstrated that GSCs preferentially cluster around tumor blood vessels, within a specialized tumor microenvironment (TME) known as the perivascular niche (PVN).[4] Beyond supplying nutrients to support tumor growth, the PVN acts as a protective sanctuary for GSCs, shielding them from immune surveillance.[5] Furthermore, the close proximity of GSCs to the capillaries within the PVN promotes infiltration of normal brain parenchyma.[6] Given the tumor-promoting role of the PVN,[3a, 7] therapeutic strategies targeting this critical and specialized niche represents a promising approach to eradicate GSCs and combat the persistence and aggressiveness of GBM.

The brain vasculature is characterized by a specialized endothelium with highly developed tight junctions that forms the blood-brain barrier (BBB), posing a major obstacle to GBM treatment by limiting the delivery of therapeutic agents to the TME.[8] Although GBM often exhibits compromised BBB due to endothelial cell (EC) dysfunction and loss of junctional integrity, the passive enhanced permeability and retention (EPR) effect remains insufficient to allow adequate therapeutic accumulation within the PVN, hindering effective administration of therapeutic regimens.[9] To address these challenges, emerging strategies employing both physical- and chemical-mediated drug delivery methods have been explored for their potential to selectively target the GBM PVN and improve the therapeutic outcomes.[10] For instance, focused ultrasound combined with microbubbles can temporarily disrupt the BBB at the tumor site, enabling localized drug delivery.[10b, 11] On the other hand, conjugating drug carriers with targeting molecules, such as RGD or angiopep-2 peptides, leverages the high expression of integrins and LRP1 receptors

T. J. M. Manoharan, T.-Y. Wang, S. Mantri, H. Alarnous, K.-C. Wang, M. Nikkhah
School of Biological and Health Systems Engineering (SBHSE)
Arizona State University
Tempe, AZ 85287, USA
E-mail: kuei-chun.wang@asu.edu; mnikkhah@asu.edu
T.-Y. Wang
School for Engineering of Matter
Transport and Energy (SEMTE)
Arizona State University
Tempe, AZ 85287, USA
S. Mehta
Ivy Brain Tumor Center
Barrow Neurological Institute
St. Joseph's Hospital and Medical Center
Phoenix, AZ 85013, USA
M. Nikkhah
Biodesign Virginia G. Piper Center for Personalized Diagnostics
Arizona State University
Tempe, AZ 85287, USA

The ORCID identification number(s) for the author(s) of this article can be found under https://doi.org/10.1002/adhm.202502454

DOI: 10.1002/adhm.202502454

on tumor-associated ECs to achieve active delivery to the GBM PVN.[9b, 12] Despite these advancements, delivering therapeutics to the GBM PVN with high precision and consistency remains a significant hurdle.[8b, 13]

One defining feature of the GBM TME is the continuous infiltration of macrophages derived from circulating monocytes, which migrate across the compromised BBB into the PVN.[14] This pathological characteristic offers a unique opportunity to specifically target the GBM PVN. Cell membrane-coated nanoparticles, which leverage the unique biomimetic properties of plasma membrane of source cells to enhance targeting, stealthiness, and biocompatibility, have garnered significant attention for improving drug delivery and have demonstrated promising results in various disease models.[15] Building on this approach, our team recently developed a monocyte membrane-coated nanoparticle (MoNP) platform capable of selectively targeting inflamed and dysfunctional ECs in atherosclerotic blood vessels while sparing healthy vascular regions. More importantly, therapeutic agents delivered by MoNP exhibited an enhanced efficacy in suppressing lesion progression compared to their free drug counterparts.[16] Given these findings and the pathological features of GBM vasculature, we hypothesized that MoNP could serve as a promising targeted delivery strategy to enhance precise delivery and drug accumulation within the PVN, enabling a more significant therapeutic effect on GBM growth and invasion.

Patient-derived xenograft (PDX) models are often considered as the gold standard for studying responses to cancer treatments, including those for GBM.[17] However, their limitation in accurately replicating the TME observed in human tumors, heterogeneity between samples, and cross-species difference restrict their ability to effectively model niche-specific tumor behavior and hampers the understanding of the impact of PVN-targeted treatments.[18] To overcome these obstacles, we have harnessed a 3D *ex vivo* tumor-on-a-chip (TOC) model, offering a more precise and reproducible mimicry of specific niches within the TME. A notable innovation is our establishment of a microfluidic GBM TOC platform with well-defined organotypic architecture. This system was previously employed to investigate interactions between patient-derived GSCs, ECs and astrocytes, revealing that both ECs and astrocytes synergistically promoted GSC migration.[19] These findings highlight the critical role of the TME components in shaping GSC behavior and reinforce the utility of the 3D TOC in mimicking the complex interactions within the GBM PVN, thus providing a relevant platform to evaluate niche-targeted therapeutics on GBM progression.[19, 20]

To advance GBM drug development, our research team integrates two complementary platforms, the MoNP delivery system and the organotypic GBM TOC model, to assess the efficacy of PVN-specific therapeutic delivery.[16,19] Specifically, the TOC features well-defined regions, including the tumor core, stroma, and a microvascular network (μVN) (**Figure 1**).[19, 20] The model stands out for its spatial organization, recapitulating the capillary structures surrounding the tumor core and stroma regions within the PVN and effectively mimicking key cell-cell interactions within a 3D extracellular matrix (ECM) environment. Further, we incorporate primary human brain microvascular endothelial cells (hBMECs), vascular pericytes (hBVPs) and patient-derived GSCs, enabling the integration of brain-specific vascular architecture surrounding GSCs to more faithfully recapitulate the GBM PVN. Leveraging this model, we utilize MoNP to deliver verteporfin (VP) to inhibit Yes-Associated Protein (YAP) signaling, which is highly activated in tumor-repopulating GSCs.[21] We evaluate the efficacy of this PVN-targeted nanodrug in suppressing invasive GSC behavior within the TOC. Our results from invasion assays, morphometric analysis, transcriptomic profiling, as well as cytokine array provide compelling evidence that MoNP-mediated VP delivery offers significant therapeutic advantages over its free-drug counterpart in treating GBM. To the best of our knowledge, this is the first study to integrate biomimetic nanomedicine with microfluidic TOC model for evaluating PVN-targeted GBM therapy.

2. Results

2.1. Establishing μVN in 3D Microfluidic TOC

The three-layered microfluidic model has three distinctive regions namely: tumor, stroma and μVN region surrounded by two flanking media channels as described in our previous studies.[19, 20, 22e] Each of these regions are separated by the presence of hexagonal and trapezoidal microposts that help in providing the necessary surface tension to hold the hydrogel in its respective region. Prior to encapsulation of tumor within the model, μVN was established as detailed in **Figure 2A**. Briefly, hBMECs and hBVPs were encapsulated in fibrin hydrogel and injected into the μVN region. The cells began to elongate and self-assemble within few days of culture and over a period of 7 days, it was evident that they showcased high random interconnected μVN as seen in the phase-contrast images (Figure 2B). Furthermore, we characterized the formed μVN with PECAM-1 (platelet endothelial cell adhesion molecule 1), an EC specific marker. Figure 2C reveals the continuous expression of PECAM-1 throughout the μVN region of the 3D TOC. Further co-staining VE-Cadherin (VE-Cad), an adherens junction protein, and alpha-smooth muscle actin (α-SMA), a marker for pericytes, revealed that the pericytes closely interact with ECs contributing to the structural integrity and development of a mature μVN (Figure 2D).[23] Furthermore, the ortho-sectioning of XZ and YZ planes clearly demonstrated the presence of well-formed, patent lumens, indicating that the ECs and pericytes had successfully organized into μVN (Figure 2E). Additionally, we conducted a time course functionality assessment to evaluate the perfusability of the μVN. Fluorescent microbeads (2 μm in diameter) were introduced into the media channel, and their movement through the network were tracked using time-lapse imaging. As shown in Figure 2F (indicated by white box) and Video S1 (Supporting Information), the microbeads successfully navigated through the vascular pathways, demonstrating the high functionality, connectivity and perfusability of the formed μVN within the chip. Collectively, these findings validate the formation of a stable and mature, characterized by perfusable lumens with highly interconnected 3D architecture suitable to conduct our further studies on tumor progression and treatment.

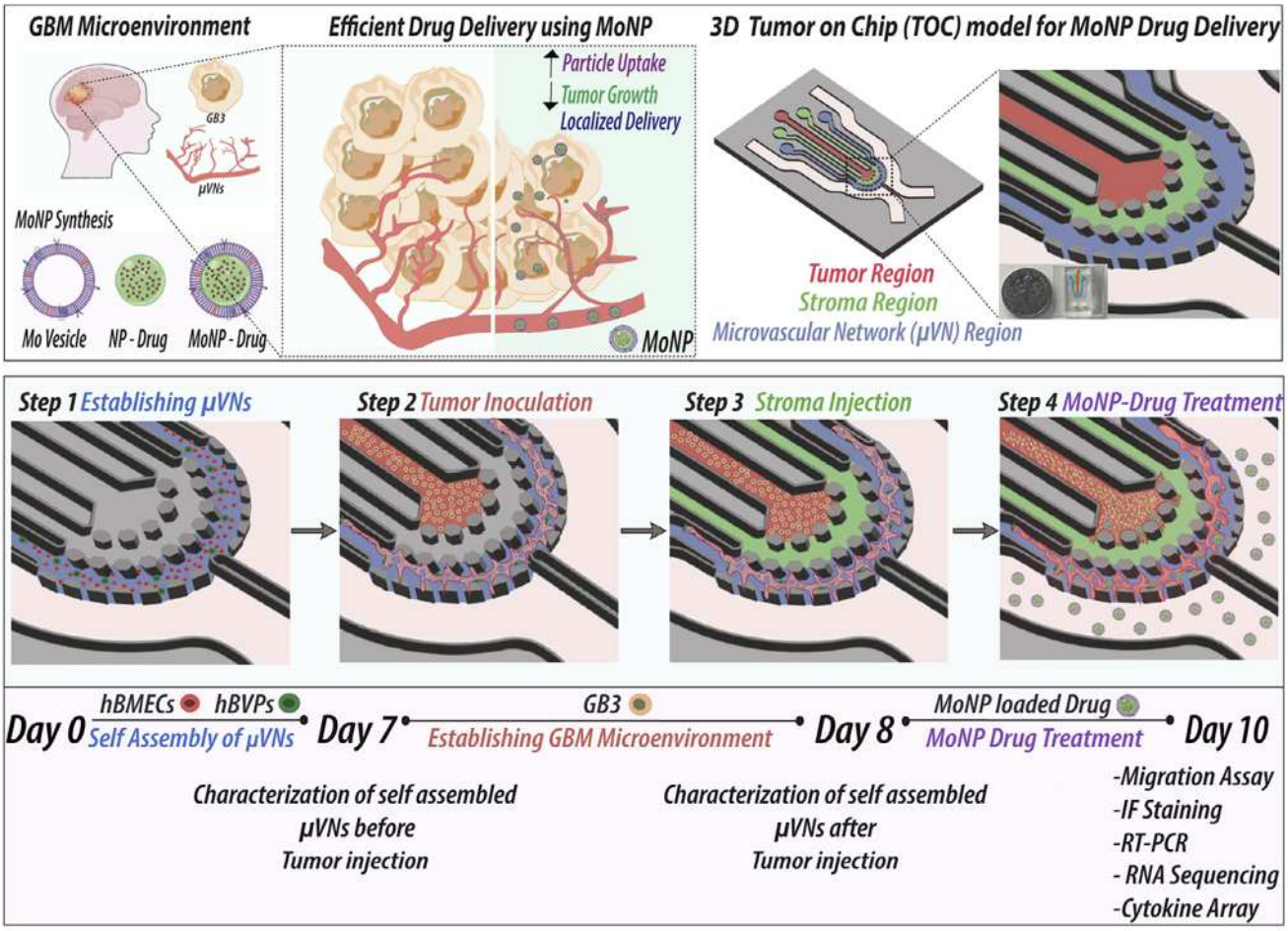

Figure 1. Overview of the Study. Schematic of the human GBM TME, which encompass the GB3 cells and μVN along with MoNP to precisely target the GBM TME [Created with Biorender.com]. Overview of the 3D TOC used for MoNP investigation, featuring distinct regions: tumor (red), stroma (green), and μVN region (blue) [Top panel]. Experimental timeline spanning 10 days, outlining four key steps: (1) formation of the μVN, (2) tumor injection, (3) stroma injection to establish the GBM TME, and (4) evaluation of MoNP-based drug delivery efficacy. [Bottom panel].

2.2. Investigating the GBM TME Influence on the Established μVN

To ensure the TOC was conducive to supporting all cell types within the TME, we first evaluated whether the culture medium affected the integrity and function of the μVN and GB3 cell behavior. Following the establishment of μVN in the EC-specific medium (i.e., EGM2-MV medium) for 7 days, the medium was switched to either neural stem cell (NSC) medium (100%) or a 1:1 ratio of NSC and EGM2-MV media (i.e., NSC+EGM2-MV cocktail). F-actin staining revealed that the NSC+EGM2-MV cocktail medium more effectively preserved vascular integrity, maintaining continuous bundles throughout the μVN region, compared to NSC medium alone (Figure 3A). Furthermore, we examined the impact on GB3 cells. After μVN establishment, GB3 cells encapsulated in Matrigel® were injected into the tumor region of the TOC, followed by addition of NSC medium alone or the cocktail medium. It was evident that in both conditions, GB3 cells exhibited significant migration into the stroma region (Figure 3B). Quantification of the migration distance showed no significant difference between both media conditions. These findings confirm that the EGM2-MV+NSC cocktail medium maintains μVN integrity while preserving GB3 behavior within the TME and was therefore selected for subsequent experiments.

Tumor cell-induced vascular dysfunction within the TME is well-documented in the literature, including in GBM and other high-grade gliomas.[24] To determine whether our TOC model recapitulates this key feature of GBM, we further investigated the impact of GB3 cell introduction on functional markers of ECs lining the μVN. Specifically, we assessed the expression of VE-Cad, a critical adherens junction protein involved in maintaining junctional integrity, and vascular cell adhesion molecule 1 (VCAM1), an adhesion molecule upregulated in activated and dysfunctional ECs. Two experimental groups were established for comparison: (i) monoculture of μVN (Mono-μVN) and (ii) co-culture of μVN with GB3 (Co-GB3+μVN). IF staining results revealed that in the monoculture group, the ECs of the μVN displayed intact adherens junctions with minimal VCAM1 expression. In contrast, co-culture with GB3, significantly downregulated VE-Cad expression with disrupted junctional integrity, and markedly increased the VCAM1-positive ECs (Figure 3C). Line intensity plot analysis showed that VE-Cad expression exhibited sharp, uniform

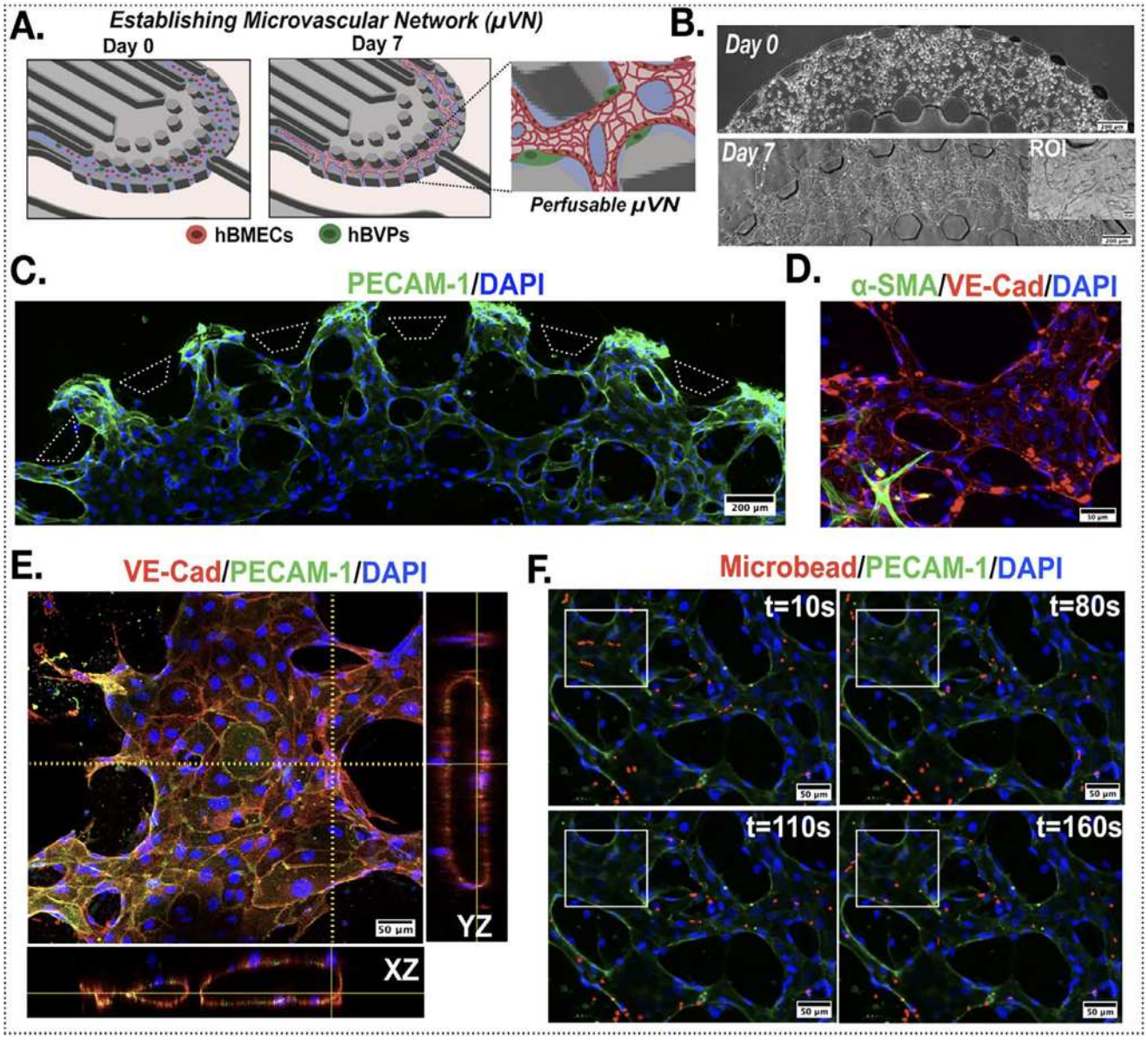

Figure 2. Establishment of μVN in the 3 layered 3D TOC Platform. A) Schematic illustration depicting the formation of the μVN within the 3D TOC over a 7-day period. B) Representative 10X tiled phase-contrast images showing the initial EC seeding (Day 0) and the formation of interconnected vascular structures by Day 7. A 20X magnified ROI on Day 7 highlights the microvascular morphology. C) Immunofluorescence (IF) staining on Day 7 showing the expression of PECAM1 (green) and nuclear counterstaining with DAPI (blue), demonstrating the formation of a continuous vascular network within the 3D TOC (Scale bar: 200 μm). D) Fluorescence image showing co-expression of α-SMA (green) and VE-Cad (red) within the formed μVN, indicating the presence of perivascular mural cells and endothelial cell-cell junctions (Scale bar: 50 μm). E) Orthogonal (XZ and YZ) views of the vascular structure obtained via confocal imaging, confirming the presence of perfusable, lumenized vessels (Scale bar: 50 μm). F) Time-lapse series (t = 10 s to t = 160 s) showing dynamic perfusion of red fluorescent microbeads through the established vascular network, with the white box highlighting successful bead movement and perfusability over time.

peaks in Mono-μVN, indicative of stable EC junctions; conversely, the Co-GB3+μVN group displayed diffuse and less pronounced peaks, reflecting disrupted junctional integrity. Quantification of VCAM1 index further confirmed this observation with a statistically significant increased expression in presence of GB3 tumor cells (Figure 3D). Moreover, we compared the dimensionality of the μVN lumen between two experimental groups. Fluorescent imaging analysis revealed that, compared to the Mono-μVN, the Co-μVN+GB3 maintained lumen width but exhibited a significantly decreased lateral diameter, indicating that the presence of tumor cells induced μVN shrinkage (Figure 3E,F). Overall, these findings suggest that co-culture with GSCs triggers μVN dysfunction in our TOC model, mimicking the compromised vasculature observed in the human GBM TME.[25]

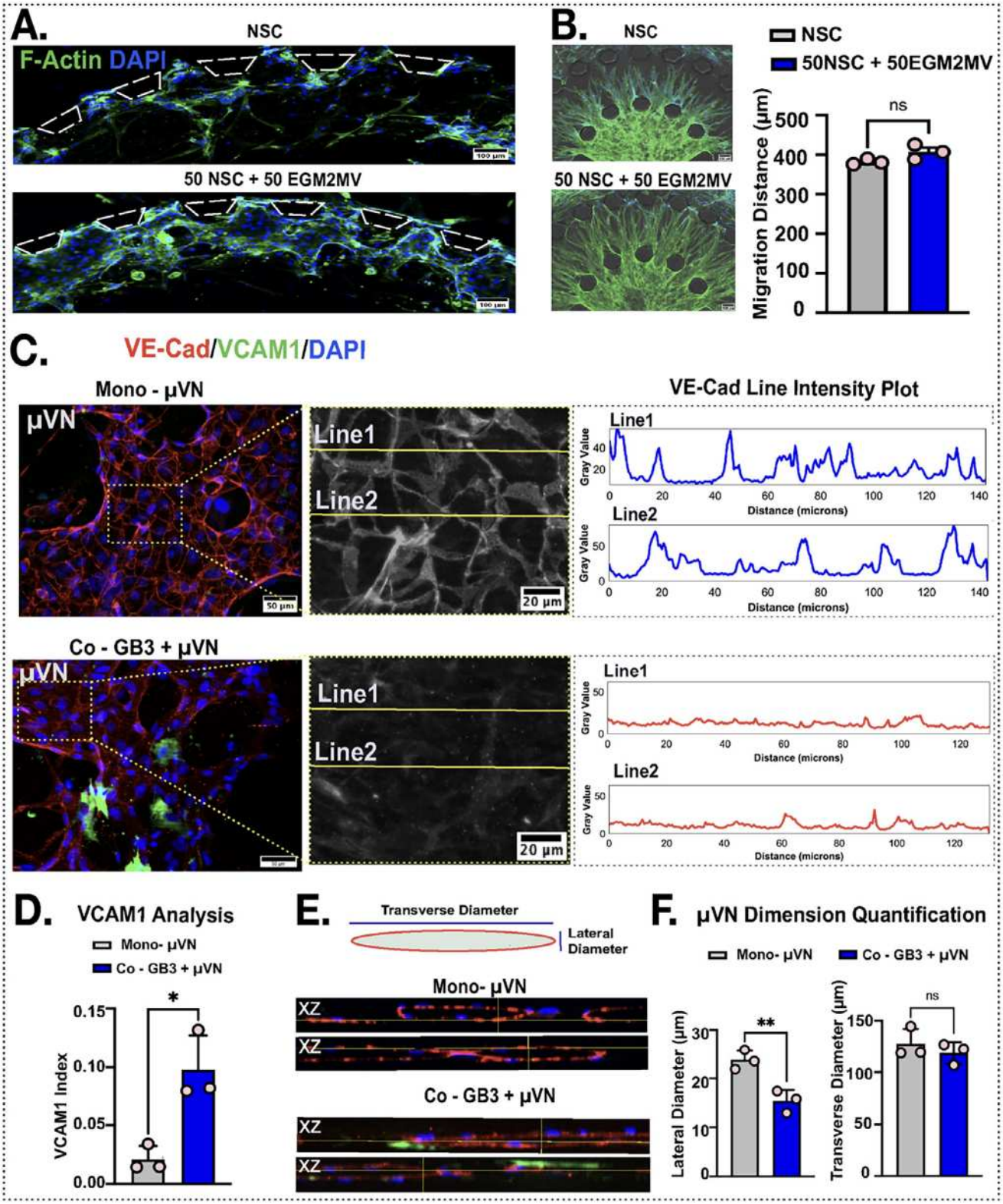

Figure 3. Investigating the Influence of the GBM TME on the Established μVN. A) Representative fluorescence images of F-actin (green) staining in the μVN region under two different media compositions, showing enhanced vascular integrity in the 50% NSC + 50% EGM2MV medium condition (Scale bar: 100 μm). B) F-actin (green) images of the tumor-stroma region showing GB3 cell migration under the same media conditions, with quantification of migration distance revealing no significant difference across the media cocktails (Scale bar: 100 μm). C) IF images of VE-Cad (red) and VCAM1 (green) expression in Mono-μVN (vascular network only) versus Co-GB3+μVN (vascular network co-cultured with GB3 cells) (Scale bar: 50 μm). Zoomed-in

2.3. Targeting GSC-Induced Dysfunctional μVN Using MoNP

After confirming the Co-GB3+μVN group faithfully replicates the GBM PVN, we proceeded to investigate whether MoNP mimic monocyte behavior by binding to and delivering their payload to the dysfunctional μVN within the TOC model. Initially, NP carrying a fluorescent payload DiD were formulated following a previously described protocol,[16] and then cloaked with plasma membranes derived from human monocytic THP1 cells to form MoNP (Figure 4A). Physicochemical characterization by dynamic light scattering (DLS) showed that the resulting MoNP had a mean hydrodynamic diameter of 234.58 nm and a zeta(ζ)-potential of -25.8 mV (Figure 4B). Successful membrane cloaking over the NP core was further confirmed by transmission electron microscopy (TEM) imaging as demonstrated in Figure 4C. Following the characterization, the uptake of fluorescently labeled MoNP (MoNP-DiD) and uncoated NP (NP-DiD) was evaluated in a 2D monolayer of hBMECs, with or without TNFα pre-treatment to induce endothelial dysfunction.[26] Quantification of intracellular fluorescent signals showed significantly higher uptake of MoNP-DiD compared to uncoated NP-DiD, with further enhancement observed in TNFα-treated hBMECs, suggesting that monocyte membrane cloaking enhanced selective nanoparticle targeting to the compromised brain endothelium (Figure S1, Supporting Information). We next evaluated the interactions of MoNP with the 3D μVN within our TOC platform. MoNP-DiD and NP-DiD were introduced into the media channel for 2 h, followed by a 24-h incubation with fresh medium. Fluorescence imaging revealed that MoNP-DiD exhibited significantly greater accumulation than NP-DiD (Figure 4D,E). Further, upon VCAM1 antibody blockade, the elevated uptake of MoNP-DiD was markedly reduced, confirming VCAM1 plays a key role in mediating MoNP interactions with ECs. Expanding on this, we extended the incubation period to 48 h, and MoNP-DiD showed enhanced penetration into the tumor–stromal interface compared to NP-DiD (Figure 4F). Z-stack images further confirmed consistent and widespread uptake of MoNP by the μVN, with pronounced DiD signals colocalized with vascular cells throughout the 3D framework indicating effective and homogeneous interaction of the MoNP (Figure 4G; Video S2, Supporting Information). Additionally, MoNP-DiD was added to μVN conditions with or without GB3 cells (Mono μVN and Co-GB3+μVN), resulting in preferential binding of MoNP-DiD to inflamed and activated ECs (Figure S2, Supporting Information). These results collectively demonstrate that MoNP significantly enhanced the selective payload delivery to the dysfunctional μVN in TOC model.

2.4. Evaluating MoNP-Mediated Delivery of VP in 3D TOC

VP, an FDA-approved drug for macular degeneration, has shown potential in treating malignancies, including GBM, by disrupting YAP activity and its downstream pro-tumorigenic gene expression.[27] Building on the preclinical success of VP in suppressing GSC behavior and GBM progression, we leveraged our TOC model to demonstrate MoNP-mediated, PVN-targeted delivery of VP for enhanced therapeutic efficacy against GBM tumors. To achieve this, VP-loaded NP cores (NP-VP) were formulated as previously reported,[16] followed by cloaking with THP1 membranes to form MoNP-VP (Figure S3A, Supporting Information). Prior to testing in our TOC model, we first treated GB3-derived spheroids with MoNP (vehicle control). RT-PCR showed no significant changes in the expression of YAP-targeted genes, including CCN1, CTGF and ANKRD1, following MoNP treatment (Figure S3B, Supporting Information), indicating that the nanoparticle alone did not affect YAP signaling. Subsequently, we incubated GB3 cells with MoNP-VP or MoNP and fluorescence imaging confirmed efficient uptake of MoNP-VP by GB3-derived spheroids/tumorspheres (Figure 5A). RT-PCR analysis further demonstrated that the MoNP-VP treatment reduced expression of YAP-targeted genes expression, confirming its effectiveness in blocking YAP-mediated transcription (Figure 5B). We next introduced MoNP-VP into the TOC model (Figure 5C). MoNP-VP, at 1, 2, and 3 μM VP-equivalent concentration, along with MoNP and free VP at 1 μM, were added to the medium channel for 2 h, followed by incubation with fresh medium for an additional 48 h. The devices were then fixed and stained with F-actin to assess the impact on the μVN and tumor core. Fluorescence imaging of the μVN region demonstrated that MoNP-VP at 1 μM was able to preserve μVN integrity, as evidenced by the open lumens observed in ortho-sectioning. In contrast, treatment with free VP at the same concentration resulted in a complete loss of vascular integrity, where no open lumens remain. However, when the VP concentration exceeded 2 μM, even with MoNP-based delivery, notable damage to μVN was observed (Figure 5D). Next, we investigated the effect on the tumor cells. F-actin staining revealed that GB3 cells exposed to the vehicle control (MoNP) exhibited migration toward the stroma, reaching the periphery of the μVN region (Figure 5E). Conversely, GB3 cells treated with MoNP-VP at all tested concentrations exhibited significantly reduced migration, remaining largely confined to the stromal layer. Notably, at 1 μM, MoNP-VP was more effective in limiting GB3 migration than free VP treatment (Figure 5G). Additionally, quantification of nuclear density (number of DAPI per Region of Interest (ROI)) and number of chains (number of branches of GB3 cells per ROI) showed significant decrease following MoNP-VP treatment (Figure S4, Supporting Information). These observations further prompted us to investigate the impact on GB3 proliferation. IF staining of Ki67 revealed a significant reduction in GB3 proliferative activity with MoNP-VP treatment but not in free VP treatment (Figure 5F,G). Importantly, no reduction in GB3 cell migration was observed when VP was delivered using uncoated NP, namely NP-VP condition (Figure 5H). These results, together, support the role of MoNP in enhancing the observed therapeutic

grayscale image of VE-Cad highlights junctional architecture (Scale bar: 20 μm), with the corresponding line intensity profile demonstrating preserved junctional continuity in the Mono-μVN condition. D) Quantification of VCAM1-positive ECs with and without GB3 co-culture, indicating GBM-induced endothelial activation via upregulation of VCAM1. E) Representative fluorescence images of μVN segments used for diameter analysis in Mono-μVN and Co-GB3+μVN conditions (Scale bar: 50 μm). F) Quantitative assessment of vessel diameters (transverse and lateral) reveals GB3-mediated morphological remodeling of the vascular network (All data are presented as mean ± SD,* indicates $p < 0.05$, ** indicates $p < 0.01$, ns indicates $p > 0.05$ calculated from Student's t-test (n = 3)).

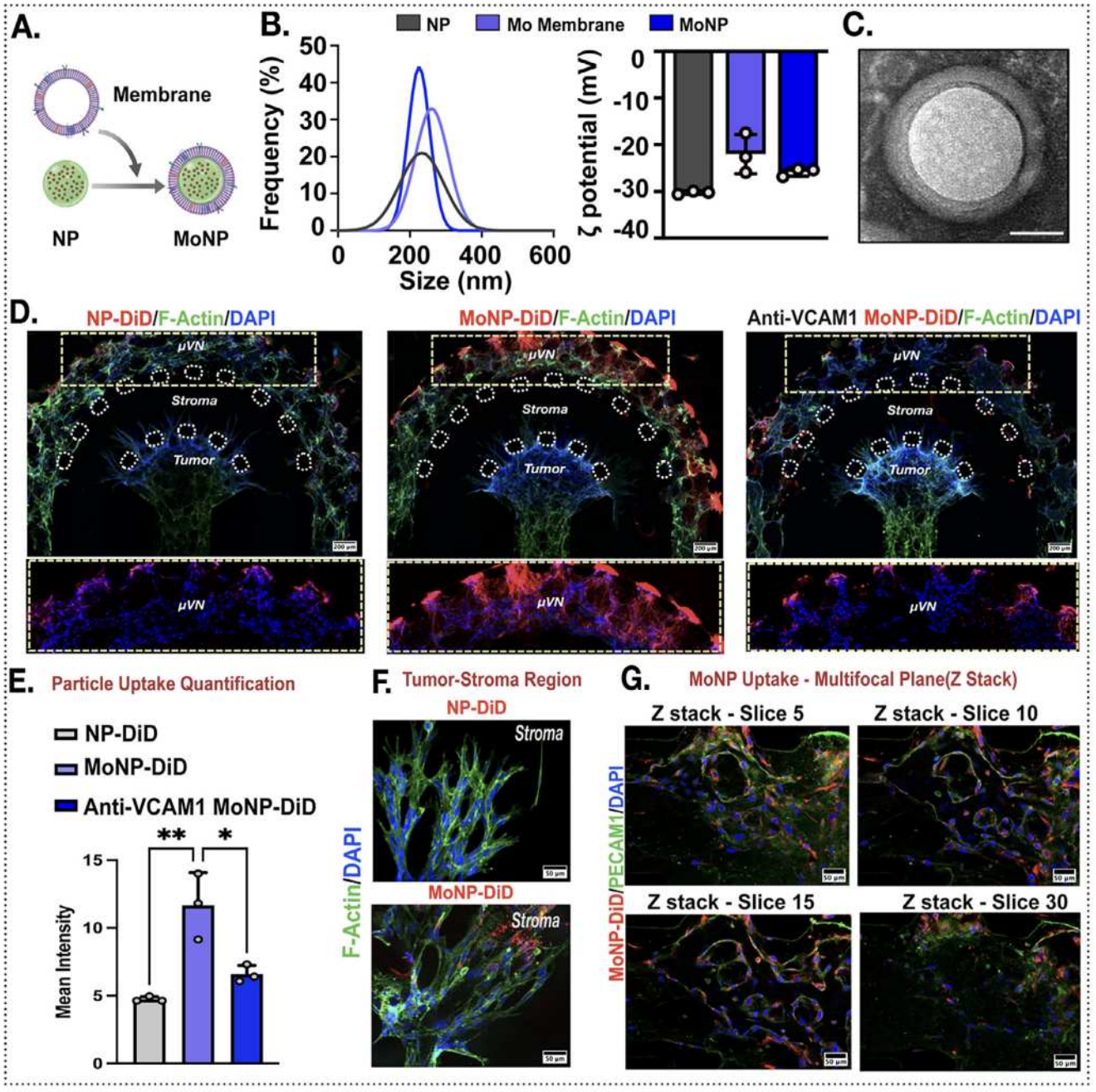

Figure 4. Targeting GB3-Induced Activated Vasculature Using MoNP. A) Schematic illustration of MoNP synthesis and functionalization [Created with BioRender.com]. B) DLS analysis showing the hydrodynamic diameter and ζ potential of MoNP confirming successful membrane coating (Data is presented as mean ± SD, (n = 3)). C) TEM image of MoNP demonstrating membrane coating on the nanoparticle surface (Scale bar: 50 nm). D,E) Fluorescence images (24-h post particle addition) (D) and quantification (E) of particle uptake in 3D TOC showing enhanced binding of MoNP-DiD to the μVN region, which is reduced following anti-VCAM1 treatment. NP-DiD/MoNP-DiD (red), F-actin (green). (Top: 4×4 tile image; Bottom: magnified view of the μVN region) (Scale bar: 200 μm). (Data is presented as mean ± SD, * indicates $p < 0.05$, ** indicates $p < 0.01$calculated from one-way ANOVA with Tukey's multiple comparison test (n = 3)). F) Representative fluorescence image (48-h post particle addition) at the tumor-stroma interface showing MoNP-DiD localization (Scale bar: 50 μm). G) Z-stack slices (Slice 5, 10, 15, and 30) from confocal imaging demonstrating progressive cellular uptake of MoNP-DiD in the μVN region. MoNP-DiD (red), PECAM1(green) (Scale bar: 50 μm).

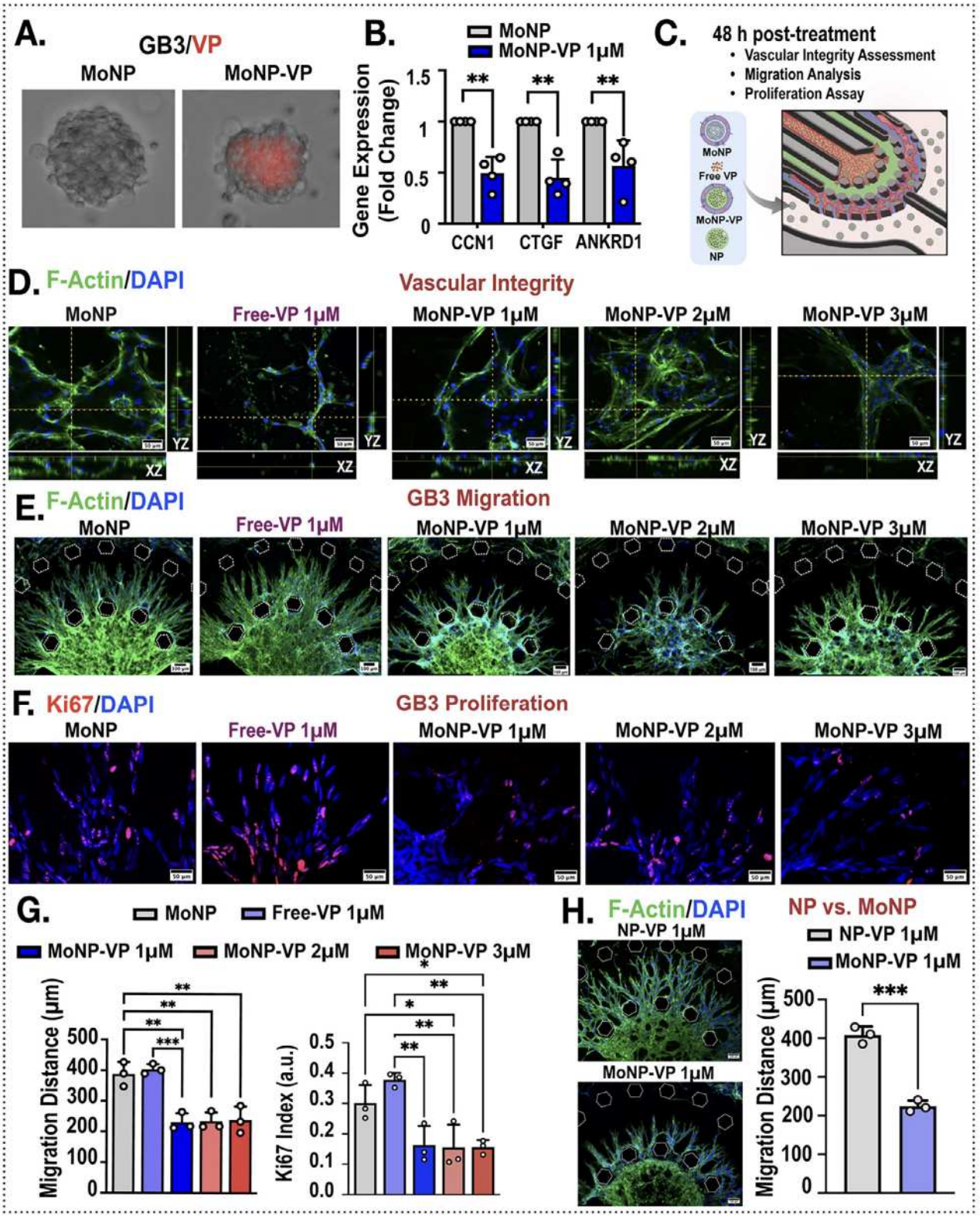

Figure 5. Targeted Delivery of VP via MoNP in the 3D TOC Model. A) Fluorescence images showing uptake of MoNP-VP [VP (red)] by GB3 cells. B) RT-PCR analysis revealing reduced YAP-related gene expression in GB3 cells treated with MoNP-VP compared to MoNP alone (Data is presented as mean ± SD, ** indicates $p < 0.01$ calculated from Student's *t*-test (n = 4)). C) Schematic overview of treatment conditions and characterization strategy within the 3D TOC platform [Created with BioRender.com]. D) F-actin (green) staining of the μVN region with orthogonal views (XZ and YZ) following various treatment conditions, demonstrating vascular integrity is intact when 1 μM VP is delivered via MoNP (Scale bar: 50 μm). E) Tiled fluorescence

efficacy of VP through targeted delivery to the PVN, rather than through passive diffusion of the free drug or nonspecific retention of uncoated nanoparticles.

2.5. Delineating the Pharmacological Mechanisms of MoNP- VP using 3D TOC

To gain further mechanistic insights into how MoNP-VP treatment impacts the GBM PVN, we extended our investigation to analyze changes in both the transcriptome and secretome of GB3 tumor cells. To accomplish this, effluents from the TOC were collected 48 h after treatment with MoNP-VP or MoNP. The μVN was subsequently removed using nattokinase digestion, and GB3 cells were harvested following the dissociation of the tumor and stroma region with collagenase II for total RNA (Figure 6A). We first assessed the expression of YAP-targeted genes in the TOC. RT-PCR analysis revealed that MoNP-VP treatment significantly reduced the expression of CCN1, CTGF, and ANKRD1 (Figure 6B), consistent with its effects on GB3-derived tumoroids (Figure 5B). Following this confirmation, total RNA from three independent biological replicates of TOCs was subjected to transcriptomic profiling via RNA-seq. Comparative analysis between MoNP-VP and MoNP treatments identified 360 differentially expressed genes (DEGs), including 291 downregulated and 69 upregulated genes (Figure S5A, Supporting Information). The top 50- and 100 DEGs are visualized in the heatmaps, highlighting the consistency across TOC replicates (Figures 6C; S5B, Supporting Information). To explore the functional relevance of the DEGs, we performed enrichment analyses using Gene Ontology (GO), Kyoto Encyclopedia of Genes and Genomes (KEGG), and Reactome databases. Selected terms from the top 20 ranked GO and pathways, included with ECM organization, collagen formation, focal adhesion, and the Hippo signaling, as shown in Figure 6D. Further Gene Set Enrichment Analysis (GSEA) analysis, notably revealed negative enrichment of these processes, indicating reduced activity following MoNP-VP treatment (Figure 6E). In parallel, conditioned media collected from the TOC devices were analyzed using a human cytokine array. Eleven out of 42 tested cytokines showing clear trends of change after MoNP-VP treatment are presented in Figure 6F, while the remaining cytokines are included in Figure S6 (Supporting Information). These differentially regulated cytokines, including ENA-78, IL-6, IL-8, IL-15, EGF, TNF-α, VEGF, MCP-1, Thrombopoietin, SDF-1 and TGF-β1, are associated with pro-inflammatory responses and are known to promote cell proliferation and migration.[28] Except for SDF-1 and VEGF, which was upregulated, the majority of the cytokines were downregulated following MoNP-VP treatment. The downregulation of these cytokines correlates with our tumor cell migration and proliferation data, supporting the anti-inflammatory and anti-proliferative effects of MoNP-VP treatment. Overall, our integrated transcriptomic and cytokine analyses, together with the phenotypic findings shown in Figure 5, suggest that MoNP-VP exerts anti-GBM effects primarily by suppressing GB3 cell interactions with the ECM and reducing the secretion of pro-inflammatory and pro-invasive cytokines (Figure 6G).

3. Discussion

The PVN serves as a critical hub that fosters dynamic interactions between GSCs and other cellular components, driving GBM progression and contributing to therapy resistance.[29] In this regard, the development of precision-targeted delivery strategies capable of selectively penetrating the PVN and disrupting tumor-supportive interactions holds immense potential for administration of effective treatment strategies for GBM. Such approaches could enhance therapeutic delivery, minimize off-target effects, and redefine the landscape of GBM treatment. While existing 2D models and PDX models have been instrumental in studying GBM, they often fail to capture the full spectrum of tumor-stroma interactions present in the human brain TME.[30] In this study, we established a 3D organotypic GBM TOC model that creates a physiologically relevant PVN, enabling the study of tumor dynamics and therapeutic responses in a well-controlled *ex vivo* experimental system. Leveraging the TOC model, we demonstrated for the first time MoNP-mediated targeting of GBM PVN. MoNP mimics the natural recruitment of monocytes to the leaky and activated vasculature of GBM, resulting in superior accumulation in the μVN of the TOC compared to passive methods. Furthermore, we demonstrated that VP, a repurposed therapeutic agent showing promise in preclinical studies for GBM, exhibited an enhanced anti-tumor efficacy when delivered via MoNP. These findings together highlight both the robustness of our GBM TOC platform and the potential of the MoNP delivery system as an effective strategy for evaluating and enhancing new therapeutic agents for GBM treatment.

Advanced 3D models—particularly microfluidic-based platforms—have emerged as powerful tools to model GBM TME and to evaluate chemotherapeutic agents.[30a, 31] In a study by Seo et al., researchers found that co-culturing glioma cell lines with the BBB led to the formation of a more complex TME, which significantly enhanced drug resistance, requiring higher concentrations of chemotherapeutic agents for effective treatment. This finding highlighted the importance of incorporating the BBB alongside GSCs to accurately recapitulate the TME in preclinical drug screening models.[32] In another recent study by Straehla et al., the team took a significant step in this direction by developing a vascularized GBM spheroid model using a microfluidic system, which exhibited permeability and vascular function comparable to the mouse brain model. Using this model, researchers assessed the therapeutic potential of functionalized liposomal nanoparticles encapsulating cisplatin,

images of the tumor-stroma region showing reduced GB3 cell migration under MoNP based VP delivery (Scale bar: 100 μm). F) IF staining of GB3 proliferation using Ki67 (red) and DAPI (blue) (Scale bar: 50 μm). G) Quantification of GB3 migration distance and Ki67 proliferation index for each treatment condition, showing significantly reduced migration and proliferation upon MoNP-based VP delivery (Data is presented as mean ± SD, * indicates $p < 0.05$, ** indicates $p < 0.01$, *** indicates $p < 0.001$ calculated from one-way ANOVA with Tukey's multiple comparison test (n = 3)). H) Comparative analysis of nanoparticle uptake between NP and MoNP (Data is presented as mean ± SD, *** indicates $p < 0.001$ calculated from Student's *t*-test (n = 3)).

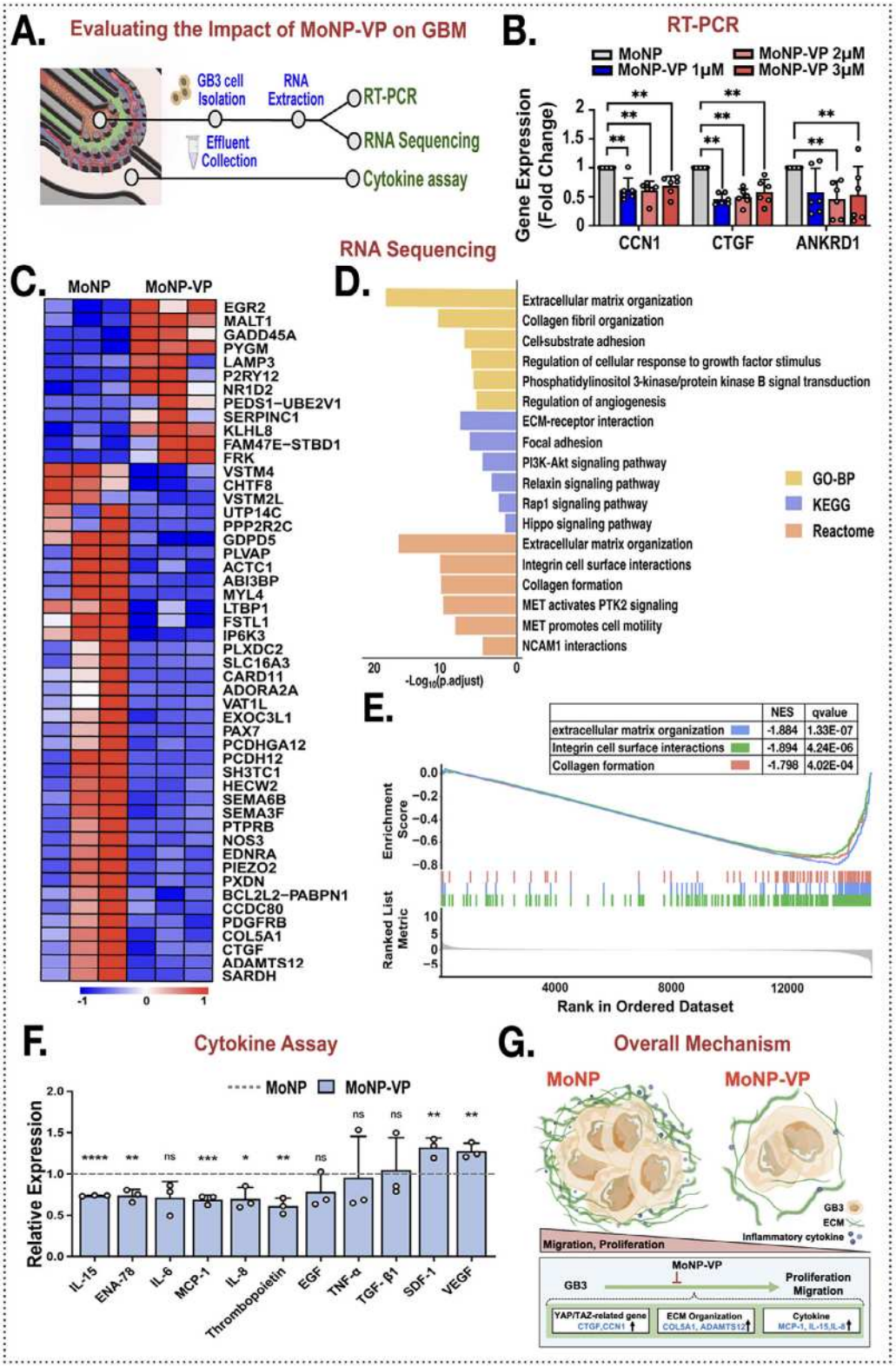

Figure 6. Evaluating the Therapeutic Impact of MoNP-VP in the 3D TOC Model. A) Schematic overview of the experimental workflow for RT-PCR, RNA-seq, and cytokine array analysis [Created with BioRender.com]. B) Gene expression levels of YAP/TAZ-related genes in GB3 cells extracted from the 3D TOC, treated with MoNP-VP or MoNP, as assessed by RT-PCR, showing reduced expression following MoNP-VP treatment (Data is presented as mean ± SD, ** indicates $p < 0.01$ calculated from Student's *t*-test ($n = 6$)). C) Heatmap showing the top 50 DEGs from RNA-seq analysis of GB3 cells treated with MoNP-VP or MoNP. D) Functional enrichment analysis of the DEGs, highlighting the top enriched GO biological processes, KEGG pathways, and

which markedly improved GBM cell killing with minimal vascular damage.[33] Although their model effectively recapitulated key aspects of the GBM TME, all cell types together were confined and distributed into a single channel, forming a central tumoroid surrounded by a complex vascular network. Alternatively, our TOC model offers spatial organotypic organization, featuring a tumor core enveloped by dense capillaries that better recapitulate the PVN. The inclusion of a defined stromal region between the tumor and vasculature enables precise investigation of cellular migration dynamics and morphology while preserving critical cell-cell interactions. Moreover, the semicircular architecture ensures more uniform drug distribution across the BBB and deeper penetration into the tumor core, thereby improving treatment assessment. Incorporating multiple ECM at different regions of the TOC, with well-defined and controlled spatial distribution, facilitates the isolation of cells from μVN and tumor-stroma region using tailored enzymatic dissociation, enabling feasible downstream molecular-level analyses. These findings establish our TOC model as a powerful tool that accurately mirrors the complex cellular interactions in glioblastoma. Numerous studies have shown that the GBM-associated vasculature is marked not only by impaired barrier function but also by endothelial activation, evidenced by the upregulation of adhesion molecules such as VCAM1.[25, 26, 34] Our TOC model faithfully recapitulates these features, with the μVN showing reduced VE-Cad and elevated VCAM1 expression in ECs during co-culture with GSCs. These findings further validate the TOC model's ability to mimic critical aspects of GBM pathophysiology, including both the invasive behavior of GSCs and the dysregulated vascular phenotype within the TME. This vascular dysfunction is also known to promote monocyte/macrophage infiltration into the TME. Consistently, the enhanced uptake of MoNP in the μVN further confirms the TOC's capability to replicate the TME but also demonstrates the potential of MoNP as an effective vascular-targeted delivery strategy for GBM. Moreover, blocking VCAM1 on hBMECs significantly reduces MoNP accumulation in μVN, further demonstrating MoNP actively interact with VCAM1 on dysfunctional ECs through monocyte membrane proteins (e.g., VLA4 integrin). This also partially supports the right-side out orientation of monocyte membranes on MoNP. Compared to conventional peptide-based approaches, such as those employing ligands for VCAM1, $\alpha v\beta 3$ integrins, or LRP1, biomimetic strategies like MoNP enable multivalent interactions with the tumor vasculature.[16] Furthermore, leveraging a patient's own monocytes to formulate MoNP, is a critical advantage and a unique feature of our delivery system, which may help enhance immune compatibility, reduce the risk of immunotoxicity associated with exogenous peptides, and support the development of a personalized drug delivery platform for GBM.[35]

Emerging evidence has revealed that dysregulation of YAP promotes GBM progression, confers resistance to radiochemotherapy, and contributes to the maintenance of GSC stemness.[36] Further, YAP drives GBM stem-like cells to become therapy-resistant and migrate toward blood vessels, allowing them to enter the PVN and sustain stemness and survival.[21] Moreover, knockdown or genetic deletion of YAP has been shown to reduce tumor size in PDX models, highlighting the therapeutic potential of targeting YAP in GBM.[27a,b, 37] Given its potency in inhibiting YAP activity, VP has been repurposed as a potential therapy for GBM.[27] Both liposomal and polymeric microparticle formulations of VP have demonstrated efficacy in PDX models in independent studies, paving the way for its ongoing clinical trials for EGFR-positive GBM.[38] However, despite its therapeutic promise, whether VP can effectively target GSCs residing in the PVN remains unknown. In addition, the development of novel formulations that can enhance targeted delivery and minimize side effects and organ toxicity associated with nonspecific YAP inhibition is clearly warranted.[39] In line with this need, we utilized the MoNP-mediated delivery to enhance the VP accumulation specifically within the GBM PVN. Our data confirmed that MoNP-VP led to superior payload retention within the PVN compared to untargeted approaches. Notably, MoNP-VP effectively reduced GB3 cell migration while preserving vascular integrity, whereas free VP at the same dose caused vascular damage and failed to suppress GB3 invasion. These findings suggest a potential limitation of passive VP formulations, as it fails to achieve sufficient accumulation within the PVN to effectively inhibit tumor cell behavior at low doses.

To evaluate whether our TOC model can capture the molecular effects of VP, we performed RNA-seq analysis on GB3 cells isolated from the devices following MoNP-VP treatment. YAP overexpression has been shown to promote GBM progression by upregulating genes involved in cell adhesion, migration, and ECM remodeling.[27b, 36c, 40] Consistent with these reports, our analysis show that MoNP-VP downregulated genes associated with ECM organization, collagen biosynthesis, and integrin-mediated interactions. Although YAP phosphorylation status and subcellular localization are key indicators of Hippo pathway activity, VP specifically functions through disrupting YAP-TEAD (Transcriptional Enhanced Associate Domain) interactions and reducing downstream transcriptional output, as reflected in the decreased expression of YAP target genes observed in our results.[41] Beyond the transcriptomic regulation, YAP has also been reported to stimulate the release of proinflammatory cytokines such as TNF-α, IL-6, IL-8, and MCP-1, creating a pro-tumorigenic TME.[42] In agreement with this, our cytokine array data demonstrated that MoNP-VP suppressed the secretion of these cytokines involved in inflammation, contributing to the observed reduction in invasive GSC behavior. Together, these findings demonstrate that our TOC platform, coupled with MoNP-mediated delivery, can effectively capture GSC responses to VP at both the transcriptomic and secretomic levels. This provides compelling evidence that the combinatory use of the 3D TOC model and MoNP platform not

Reactome pathways. E) GSEA comparing MoNP-VP to MoNP-treated GB3 cells, showing NES and q-values. F) Secretome profiling of 11 cytokines, revealing MoNP-VP-induced alterations in the GBM TME. (n = 3) (Data is presented as mean ± SD, * indicates $p < 0.05$, ** indicates $p < 0.01$, *** indicates $p < 0.001$, **** indicates $p < 0.0001$ calculated from Student's *t*-test (n = 3)). G) Proposed mechanism of MoNP-VP action on GB3 cells based on transcriptomic and secretomic profiling [Created with BioRender.com].

only enables robust evaluation of therapeutic responses but also facilitates mechanistic dissection of drug action within a physiologically relevant GBM TME.

The PDX model is a well-established and essential platform for validating the therapeutic efficacy of anticancer agents by implanting human tumors into immunocompromised mice, thereby preserving tumor heterogeneity and mimicking interactions with the TME.[43] However, our TOC model offers distinct advantages and should be viewed as complementary to, rather than a replacement for, the PDX model. The TOC platform is specifically designed for rapid drug screening and mechanistic studies in a controlled microenvironment. Compared to PDX models, the TOC platform reduces systemic variability associated with host factors and provides a more defined and reproducible setting for studying pharmacodynamic responses. In our study, MoNP-VP treatment significantly suppressed tumor cell growth and invasion in the TOC model. This effect is consistent with previous reports showing that VP reduces tumor size in PDX models of GBM.[27b] While the TOC and PDX systems differ in complexity and biological context, the consistent therapeutic effect of VP observed across both platforms highlights its robust antitumor potential and supports the successful establishment of the TOC model as a viable screening platform. Importantly, the enhanced efficacy of MoNP-VP in our TOC model further underscores the translational relevance of this targeted nanotherapeutic strategy for GBM.

Building on this work, our future studies will incorporate patient-derived GSCs harboring diverse oncogenic drivers (e.g., EGFR amplification, TP53 mutation) to address GBM heterogeneity, as well as evaluate whether MoNP can enhance therapeutic responses of GSCs within the TOC model to both novel agents and existing chemotherapeutics with limited BBB permeability. Additional enhancements include the integration of immune cells, such as macrophages and T cells, along with other stroma components, to create a more physiologically relevant platform for the precise evaluation of therapeutic agents. We believe that employing this TOC-MoNP system will accelerate drug screening applications and support the development of a high-throughput platform to evaluate tumor responses, paving the way for the advancement of personalized precision nanomedicine for GBM.

4. Conclusion

In summary, we have developed a highly physiologically relevant and organotypic 3D GBM TOC model, integrated with an effective vascular-targeted delivery system MoNP, to address key limitations of conventional preclinical models and targeted drug delivery approaches. Our findings demonstrate that the TOC platform accurately recapitulates the complex features of the GBM PVN. Notably, MoNP exhibited enhanced accumulation within the PVN, and when loaded with VP, effectively targeted activated vasculature and achieved greater inhibition of GSC growth and invasiveness as compared to the free drug. This innovative integration establishes the TOC-MoNP system as a powerful and translatable platform for targeted drug screening, mechanistic exploration, and the development of personalized therapeutic strategies for GBM.

5. Experimental Section

Cell Culture: hBMECs (Cell Systems, #ACBRI 376) were maintained at passages 7 to 11 were used for the study. The cells were cultured on the flask coated with attachment factor (#4Z0-201) in complete classic medium with serum and culture boost (#4Z0-500) as per the manufacturer's instruction. hBVPs (ScienCell, #1200) were cultured in pericytes medium (#1201) on a poly-L-lysine (Sigma) coated flask. The cells at passage 3–9 were used for the experiments. Human THP-1 monocytes (ATCC) were cultured in RPMI 1640 medium supplemented with 10% fetal bovine serum and 1% Pen-Strep (Fisher Scientific).

A GSC cell line (GB3-RFP), referred as GB3 in this study, was generated by Dr. Mehta's laboratory and were established from resected GBM tumor tissue obtained by the Biobank Core Facility at St. Joseph's Hospital and Medical Center and the Barrow Neurological Institute in Phoenix, Arizona. The samples were anonymized and adhered to the Institutional Review Board protocol (IRB tracking number – 20200850). GB3 cells were cultured and propagated following previously published protocols.[19] Briefly, the cells were cultured as spheroids in a NSC medium. This medium included Dulbecco's Modified Eagle Medium and F12-Glutamax, with supplements of N2 (Gibco, #17502048), B27 (Gibco, #17504044), and Pen-Strep (Fisher Scientific). The cells were treated with 20 ng mL^{-1} of epidermal growth factor (EGF, Sigma, #PHG0311L) and 20 ng mL^{-1} of fibroblast growth factor (FGF, EMD Millipore #01-106) every other day until they became confluent. Cells with passage number less than 30 were used for the experiments. All cells used in this study were kept in a humidified incubator at 37 °C with 5% CO_2, and the culture medium was refreshed every 2 days.

Device Fabrication and Surface Treatment: The fabrication of the microfluidic TOC was similar to our previous studies.[19, 20, 22] Initially, the device was designed using CAD software and transferred onto a transparent mask. Next, a layer of negative photoresist SU8-2075 (MicroChem) was applied to a silicon wafer, achieving a thickness of 200 µm. The transparent mask was precisely aligned and exposed to UV light to create master mold with the desired features. For the soft-lithography procedure, to ensure the silicon wafer's integrity during device removal, the master silicon mold underwent treatment with methyl trichlorosilane (MTCS-Sigma-Aldrich). Next, polydimethylsiloxane (PDMS) mixed with the curing agent (Sylgard 184 Silicon Elastomer Kit, Dow Corning) in a 10:1 ratio was poured onto the wafer. The poured mixture was degassed in a vacuum desiccator to remove the trapped air bubbles. The mixture was baked at 80°C for 1.5 h and subsequently, the PDMS layer was carefully peeled off from the silicon wafer and was cut into individual devices. Inlets and outlets were created using 1- and 1.5-mm biopsy punches, ensuring precise access points for fluid handling within the devices. The bonding of each microfluidic device to glass slide ensured the creation of completely sealed environments. For which, glass slides were prepared by cleaning with ethanol. The device along with the glass slide, were treated with oxygen plasma (PDC-32G, Harrick Plasma) prior to bonding. By hydrophilizing the surface, it enabled effective bonding of the glass slide with devices positioned channel-side down, ensuring the complete formation of channels. Following this, the devices were incubated at 80 °C overnight to enhance bonding as well as to restore the hydrophobicity of the device. Lastly, for sterilization, the devices underwent a liquid autoclave cycle followed by a dry cycle, after which they were left at 80 °C overnight to ensure complete drying.

To optimize conditions for cell culture and ensure proper hydrogel attachment, the devices underwent surface treatment. Initially, the cell culture zones were coated with 1 mg mL^{-1} of poly-D-lysine (Sigma-Aldrich) and incubated at 37 °C for 1.5 h. Subsequently, the devices were rinsed once with deionized (DI) water. Following this step, glutaraldehyde (1% v/v) (Sigma-Aldrich) was added and allowed to incubate for 2 h at room temperature (RT), followed by thorough washing with DI water (3–5 times). The surface-treated devices were then left at 80 °C overnight to restore their hydrophobic properties.

Establishment of µVN in Microfluidic TOC Device: To establish vasculature in the third layer of the microfluidic device, hBMECs and hBVPs were dissociated using Trypsin-EDTA. Next, 6 mg mL^{-1} bovine fib-

rinogen (Sigma, #F8630-1G) was prepared by dissolving it in Dulbecco's phosphate-buffered saline (PBS, Gibco). Simultaneously, bovine thrombin (Sigma, #T4648-1KU) was prepared in EGM-2-MV media at a concentration of 4 IU mL^{-1}. Both the fibrinogen and thrombin preparations were filter-sterilized using 0.2 µm filter and was kept on ice.

Prior to adding the cells, equal volumes of fibrinogen and thrombin were mixed and kept at RT for 10 min to ensure hydrogel crosslinking. Once the hydrogel crosslinking efficiency has been checked, cell pellets of hBMECs and hBVPs were resuspended in the thrombin mixture at concentrations of 64.8 million (M) cells mL^{-1} and 7.2 M cells mL^{-1}, respectively. Finally, a mixture of 1:1:2 ratio of hBMECs in thrombin, hBVPs in thrombin, and fibrinogen was prepared to achieve a final cell concentration of 16.2 M cells mL^{-1} for hBMECs and 1.8 M cells mL^{-1} for hBVPs, resulting in a total cell concentration of 18 M cells mL^{-1}. The prepared cell mixture was injected into the third layer of the microfluidic TOC device. The devices were crosslinked for 10 min at RT. Once crosslinked, EGM-2-MV media supplemented with 50 ng mL^{-1} of vascular endothelial growth factor (VEGF, Sigma, #V7259) was added to the two flanking media channels. The devices were maintained in a humidified chamber under optimal cell culture conditions (5% CO_2, 37 °C). The media was exchanged every 24 h for up to 7 days.

Establishing Invasion Assay Using Microfluidic Platform: To assess the GSC invasion and phenotype within the microfluidic platform, patient derived GB3-RFP cells referred to as GB3 hereafter, were injected into the tumor region of the device upon establishing vasculature for 7 days. Briefly, GB3 spheroids were collected, centrifuged at 800 rotations per minute (RPM) for 5 min, and dissociated into single cells using Accutase (Gibco, # A1110501). The dissociated cells were encapsulated in Matrigel® (Corning, #47743-706) at a final concentration of 15 M cells mL^{-1}. This mixture was injected into the tumor region of the device and was allowed to crosslink for 6–7 min at 37 °C. The devices were flipped every 2 min once to ensure they were homogenously spread across the 3D platform. Once crosslinked, Matrigel® was added to the stroma region and was crosslinked for 8 min. After which the media was switched to the cocktail medium (50% EGM2-MV + 50% NSC medium).

Nanoparticle Synthesis and Characterization: Ten milligrams of poly (D, L-lactide-co-glycolide) (PLGA; Resomer RG 503H, Sigma Aldrich), alongside 400 µg of DiD (Biotium) or 2 mg of VP (Tocris Bioscience), were dissolved in 1 mL of dichloromethane (DCM, Sigma Aldrich) and processed following a single emulsion method to formulate the NP cores.[16] Monocyte membranes, isolated from THP1 cells using a Minute Membrane Protein Isolation kit (Invent Biotechnologies), were added to NP cores at a membrane proteins-to-cores weight ratio of 1:10 and dispersed in an ultrasonic bath to form MoNP. The physicochemical properties of MoNP were characterized using DLS and TEM. VP-loaded NP cores were lyophilized and then dissolved in dimethylsulfoxide. The fluorescence intensity was measured at 690 nm using a plate reader (BioTek) to calculate the encapsulation efficiency (EE%) and loading efficiency (LE%), as described previously.[16]

Nanoparticle Uptake Studies in Microfluidic Platform: As an initial step to investigate MoNP uptake within the microfluidic platform, GB3 cells were injected into the tumor region after µVN formation and cultured for 24 h. Subsequently, MoNP and uncoated NP loaded with DiD were injected into media channels devices were treated with the particles for 2 h, after which unattached particles were removed by washing with the media for at least 4 times. For the VCAM1 blocking experiments, the TOC devices were pre-incubated with a media cocktail containing anti-VCAM1 antibody (1:20 dilution) for 3 h prior to nanoparticle addition. The antibody solution was introduced through the media channel to enable effective VCAM1 blockade. Following nanoparticle treatment, devices were either fixed at 24 h using 4% paraformaldehyde (PFA) for analysis or, in some instances, fixed at 48 h to assess extended particle retention and distribution. VP-loaded MoNP were administered and analyzed in the same manner to assess their functional outcomes.

Immunofluorescence Staining: The devices were initially washed with PBS. Following this, the cells were fixed with 4% PFA for 30 min at 37 °C. Subsequently, the devices underwent 2 washes with PBS-glycine (100 mM glycine in PBS) for 5 min at RT. A final wash was done with PBS-Tween-20 (PBST) (0.05% v/v Tween-20 in PBS) for 10 min. Cells were permeabilized with 0.1% Triton X-100 in PBST for 30 min at RT. Following permeabilization, a blocking buffer (10% goat serum in PBST) was added and incubated for 1 h to prevent non-specific antibody binding. The devices were then incubated with primary antibodies at 4 °C overnight, diluted in 1:1 ratio of 10% goat serum and 0.1% Triton-X-100. The antibodies used in this study and their dilution factors are listed in Table S1 (Supporting Information). After incubation with primary antibodies and washes with PBST, corresponding secondary antibodies (Alexa Fluor 488/555/647) were added at a 1:500 dilution, along with 4′,6-diamidino-2-phenylindole (DAPI, 1:1000 dilution, Invitrogen) solution. In the case of using fluorescently labeled primary antibodies, the devices were washed 2–3 times with PBST for 10 min at RT, followed by counterstaining with DAPI.

Data Acquisition and Analysis: A Zeiss Axio Observer Z1 microscope, equipped with an Apotome2 system (Zeiss) and Zen Pro software, was used to capture phase-contrast and fluorescence images. In some cases, BioTek Lionheart LX automated microscope as well as the Leica SP8 Confocal Microscope at 20X objective (ASU RegenMed Core Facility) was utilized. During the course of experiment, phase-contrast images were acquired before and after drug treatment using a 10X objective with a 4×4 tile configuration. IF images were obtained at 10X and 20X magnifications. For 3D reconstruction, z-stack imaging was performed across multiple focal planes.

The VCAM1 index and Ki67 index was determined using the formula below, with manual counting conducted for accuracy. For each condition, three images were analyzed, and with three biological replicates, a total of 9 images were used for the VCAM1 and Ki67 index assessment.

$$\text{VCAM1 index} = \frac{\text{Number of VCAM1 positive cells}}{\text{Total Number of Nuclei in the Field of view}} \quad (1)$$

$$\text{Ki67 index} = \frac{\text{Number of Ki67 positive cells}}{\text{Total Number of Nuclei in the Field of view}} \quad (2)$$

Similarly, the cell junctions were analyzed using intensity-based line plot profile from ImageJ. For the transverse and lateral diameter, for each condition namely (i) Mono µVN and (ii) Co-GB3+µVN— three ROIs per biological replicate were imaged. From each Z-stack acquired ROI image two measurements were extracted for both transverse and lateral vessel diameters. The transverse diameter (width of the lumen), lateral diameter (height of the lumen) and the migration analysis were measured using line segment tool. F-Actin-stained fluorescent images acquired was used to quantify the chain migration. The number of chains per field of view (FOV) and nuclei per FOV was counted manually.

RNA Extraction for RT-PCR and RNA -seq – Process and Analysis: Forty-eight hours post MoNP treatment, the devices were washed with PBS, and nattokinase (70 fibrinolytic units in 1 mM EDTA in PBS) was added to the media channel to dissociate vascular cells from the µVN regions. After confirming the complete removal of cells from the µVN, collagenase type II (2 mg mL^{-1} in 1 mM EDTA in PBS) was added to the media channel. The devices were then incubated at 37 °C for 20 min to collect GB3 cells from the tumor and stroma region. Swiftly after GB3 isolation, total RNA was extracted using a RNeasy UCP Micro Kit (Qiagen) for subsequent RT-PCR analysis and transcriptomic profiling. For RT-PCR analysis, RNA was reverse-transcribed with oligo-dT primer (Promega) and M-MLV reverse transcriptase (Promega). RT-PCR was then performed on a CFX Duet Real-Time PCR System (Bio-Rad). Relative gene expression levels were calculated using the $2^{-\Delta\Delta CT}$ method. Primer sequences are provided in Table S2 (Supporting Information). For transcriptome profiling, the preparation of cDNA library and transcriptome sequencing were conducted by Novogene. The sequence reads were aligned to the reference human genome (hg38) using STAR,[44] and gene-level read counts were quantified with StringTie.[45] Differential gene expression was determined using DESeq2,[46] with genes having a total count of fewer than 10 across all samples removed prior to the analysis. A heatmap was generated using pheatmap (version 1.0.12) based on row z-score value. DEGs with a multiple hypotheses-corrected P value of <0.05 and $|\log_2(\text{fold change})| \geq 0.5$ were considered up-regulated or down-regulated. Functional enrichment

analysis, including KEGG, Reactome, GO, and GSEA, was performed using ClusterProfiler.[47] RNA-seq data are available in the GEO database under the accession number GSE294720.

Cytokine Array: Forty-eight hours after MoNP treatment, the effluents collected from the devices were pooled by condition and subjected to cytokine secretion analysis. Raybiotech's human cytokine antibody array (Cat# AAH-CYT-G3) was utilized. All the steps were followed as per the manufacturer's interaction. Signal intensities were background-corrected and normalized using the positive and negative controls included on the array. Untreated media served as the control, and all data were initially normalized to this condition. To specifically assess the effect of VP, a secondary normalization was performed using the MoNP group as the reference. Table S3 (Supporting Information) includes the data from three independent biological replicates.

Statistical Analysis: All the data values were derived from at least three independent experiments for comprehensive analysis. All the results and data were presented as mean ± standard deviation (mean ± SD). Statistical significance was evaluated using Student's *t*-test and one-way analysis of variance (ANOVA) with Tukey's multiple comparison. Analyses were performed using GraphPad Prism software (GraphPad Prism 10), and a p value < 0.05 was considered statistically significant.

Supporting Information

Supporting Information is available from the Wiley Online Library or from the author.

Acknowledgements

T.M and T.-Y.W. contributed equally to this work. S.M. and H.A. contributed with the 2D optimization studies. Some part of Figures 1 and 6 were partly created using figures provided by Servier Medical Art (https://smart.servier.com/), licensed under a Creative Commons Attribution 4.0 Unported License. SM provided GB3 cells and guidance with GSC studies. All authors reviewed and proofread the manuscript. K.W. would like to acknowledge support from NIH award R00HL135416, which contributed to the early development of the nanoparticles. M.N. would like to acknowledge NIH award R01NS123038 and NSF CBET #2309859 for supporting this work, specifically on the development and biological characterizations of GBM TOC model system. K.W. and M.N. would like to acknowledge the Arizona Biomedical Research Centre for supporting this work through award #RFGA2024-022-027 – MPO20250016.

Conflict of Interest

The authors declare no conflict of interest.

Data Availability Statement

The data that support the findings of this study are available from the corresponding author upon reasonable request.

Keywords

glioblastoma multiforme (GBM), microfluidics, nanomedicine, targeted delivery, tumor-on-a-chip

Received: July 14, 2025
Revised: August 22, 2025
Published online:

[1] a) F. Hanif, K. Muzaffar, K. Perveen, S. M. Malhi, U. S. Sh, *Asian Pac. J. Cancer Prev.* **2017**, *18*, 3; b) D. Sipos, B. L. Raposa, O. Freihat, M. Simon, N. Mekis, P. Cornacchione, Á. Kovács, *Cancers* **2025**, *17*, 146.
[2] a) A. P. Ghiaseddin, D. Shin, K. Melnick, D. D. Tran, *Curr. Treat. Options Oncol.* **2020**, *21*, 76; b) B. Oronsky, T. R. Reid, A. Oronsky, N. Sandhu, S. J. Knox, *Front. Oncol.* **2020**, *10*, 574012; c) A. Shergalis, A. BankheadIII, U. Luesakul, N. Muangsin, N. Neamati, *Pharmacol. Rev.* **2018**, *70*, 412; d) O. G. Taylor, J. S. Brzozowski, K. A. Skelding, *Front. Oncol.* **2019**, *9*, 963.
[3] a) B. C. Prager, S. Bhargava, V. Mahadev, C. G. Hubert, J. N. Rich, *Trends Cancer* **2020**, *6*, 223; b) R. C. Gimple, S. Bhargava, D. Dixit, J. N. Rich, *Genes Dev.* **2019**, *33*, 591.
[4] a) J. M. Heddleston, M. Hitomi, M. Venere, W. A. Flavahan, K. Yang, Y. Kim, S. Minhas, J. N. Rich, A. B. Hjelmeland, *Curr. Pharm. Des.* **2011**, *17*, 2386; b) A. Mosteiro, L. Pedrosa, A. Ferrés, D. Diao, À. Sierra, J. J. González, *Biomedicines* **2022**, *10*, 1285; c) N. A. Charles, E. C. Holland, *Cell Cycle* **2010**, *9*, 3084.
[5] a) D. A. Aderetti, V. V. V. Hira, R. J. Molenaar, C. J. F. van Noorden, *Biochim Biophys Acta Rev Cancer* **2018**, *1869*, 346; b) D. Schiffer, L. Annovazzi, C. Casalone, C. Corona, M. Mellai, *Cancers (Basel)* **2018**, *11*, 5.
[6] a) J. Wang, Y. Ma, M. K. Cooper, *Transl Cancer Res* **2013**, *2*, 429; b) T. G. Agnihotri, S. Salave, T. Shinde, I. Srikanth, V. Gyanani, J. C. Haley, A. Jain, *Journal of the National Cancer Center* **2023**, *3*, 222.
[7] a) N. Charles, E. C. Holland, *Cell Cycle* **2010**, *9*, 3084; b) V. V. V. Hira, D. A. Aderetti, C. J. F. van Noorden, *J. Histochem. Cytochem.* **2018**, *66*, 349; c) M. D. Brooks, R. Sengupta, S. C. Snyder, J. B. Rubin, *Curr. Pathobiol. Rep.* **2013**, *1*, 101; d) G. Seano, *Curr Opin Oncol* **2018**, *30*, 54.
[8] a) E. ter Linden, E. R. Abels, T. S. van Solinge, J. Neefjes, M. L. D. Broekman, *Cells* **2024**, *13*, 998; b) I. Noorani, J. de la Rosa, *Nat. Commun.* **2023**, *14*, 5909.
[9] a) S. S. Kim, J. B. Harford, K. F. Pirollo, E. H. Chang, *Biochem. Biophys. Res. Commun.* **2015**, *468*, 485; b) S. Zha, H. Liu, H. Li, H. Li, K.-L. Wong, A. H. All, *ACS Nano* **2024**, *18*, 1820.
[10] a) S. Trivedi, V. Bhoyar, N. Akojwar, V. Belgamwar, *Nano Trends* **2023**, *1*, 100005; b) E. N. Mathew, B. C. Berry, H. W. Yang, R. S. Carroll, M. D. Johnson, *Int. J. Mol. Sci.* **2022**, *23*, 1711.
[11] A. Burgess, K. Shah, O. Hough, K. Hynynen, *Expert Rev. Neurother.* **2015**, *15*, 477.
[12] D. Nikitovic, E. Kukovyakina, A. Berdiaki, A. Tzanakakis, A. Luss, E. Vlaskina, A. Yagolovich, A. Tsatsakis, A. Kuskov, *Cancers* **2024**, *16*, 3768.
[13] a) E. N. Mathew, B. C. Berry, H. W. Yang, R. S. Carroll, M. D. Johnson, *Int. J. Mol. Sci.* **2022**, *23*, 1711; b) W. H. Bae, S. Maraka, A. Daher, *Front. Oncol.* **2024**, *14*, 2024.
[14] a) D. Hambardzumyan, G. Bergers, *Trends Cancer* **2015**, *1*, 252; b) D. F. Quail, J. A. Joyce, *Cancer Cell* **2017**, *31*, 326; c) D. Friedmann-Morvinski, D. Hambardzumyan, *J. Clin. Invest.* **2023**, *133*, e163451.
[15] a) R. H. Fang, A. V. Kroll, W. Gao, L. Zhang, *Adv. Mater.* **2018**, *30*, 1706759; b) S. Zou, B. Wang, C. Wang, Q. Wang, L. Zhang, *Nanomedicine (Lond)* **2020**, *15*, 625; c) N. Desai, V. Tambe, P. Pofali, L. K. Vora, *Advanced NanoBiomed Research* **2024**, *4*, 2400012; d) Y. He, S. Zhang, Y. She, Z. Liu, Y. Zhu, Q. Cheng, X. Ji, *Exploration* **2024**, *4*, 20230164; e) V. Chugh, K. Vijaya Krishna, A. Pandit, *ACS Nano* **2021**, *15*, 17080.
[16] H. C. Huang, T. Y. Wang, J. Rousseau, M. Orlando, M. Mungaray, C. Michaud, C. Plaisier, Z. B. Chen, K. C. Wang, *Biomaterials* **2024**, *306*, 122505.
[17] N. Yadav, B. W. Purow, *J Neurooncol* **2024**, *166*, 213.
[18] S. Abdolahi, Z. Ghazvinian, S. Muhammadnejad, M. Saleh, H. Asadzadeh Aghdaei, K. Baghaei, *Journal of Translational Medicine* **2022**, *20*, 206.

[19] E. A. Adjei-Sowah, S. A. O'Connor, J. Veldhuizen, C. Lo Cascio, C. Plaisier, S. Mehta, M. Nikkhah, *Adv. Sci. (Weinh)* **2022**, *9*, 2201436.
[20] D. Truong, R. Fiorelli, E. S. Barrientos, E. L. Melendez, N. Sanai, S. Mehta, M. Nikkhah, *Biomaterials* **2019**, *198*, 63.
[21] C. Pichol-Thievend, O. Anezo, A. M. Pettiwala, G. Bourmeau, R. Montagne, A.-M. Lyne, P.-O. Guichet, P. Deshors, A. Ballestín, B. Blanchard, J. Reveilles, V. M. Ravi, K. Joseph, D. H. Heiland, B. Julien, S. Leboucher, L. Besse, P. Legoix, F. Dingli, S. Liva, D. Loew, E. Giani, V. Ribecco, C. Furumaya, L. Marcos-Kovandzic, K. Masliantsev, T. Daubon, L. Wang, A. A. Diaz, O. Schnell, et al., *Nat. Commun.* **2024**, *15*, 3602.
[22] a) T. J. M. Manoharan, K. Ravi, A. P. Suresh, A. P. Acharya, M. Nikkhah, *Adv. Healthcare Mater.* **2024**, *13*, 2303658; b) D. D. Truong, A. Kratz, J. G. Park, E. S. Barrientos, H. Saini, T. Nguyen, B. Pockaj, G. Mouneimne, J. LaBaer, M. Nikkhah, *Cancer Res.* **2019**, *79*, 3139; c) N. Peela, E. S. Barrientos, D. Truong, G. Mouneimne, M. Nikkhah, *Integrative Biology* **2017**, *9*, 988; d) K. Ravi, Y. Zhang, L. Sakala, T. J. M. Manoharan, B. Pockaj, J. LaBaer, J. G. Park, M. Nikkhah, *Adv. Sci.* **2025**, *12*, 2413457; e) S. Nagaraju, D. Truong, G. Mouneimne, M. Nikkhah, *Adv. Healthcare Mater.* **2018**, *7*, 1701257.
[23] a) M. Campisi, Y. Shin, T. Osaki, C. Hajal, V. Chiono, R. D. Kamm, *Biomaterials* **2018**, *180*, 117; b) H. Zhao, J. C. Chappell, *J. Biol. Eng.* **2019**, *13*, 26.
[24] a) C. Pacheco, C. Martins, J. Monteiro, F. Baltazar, B. M. Costa, B. Sarmento, *Frontiers in Drug Delivery* **2022**, *2*, 823412. b) Y. Hu, Z. Li, Y. Zhang, Y. Wu, Z. Liu, J. Zeng, Z. Hao, J. Li, J. Ren, M. Yao, *Int J Biol Sci* **2023**, *19*, 4311.
[25] Y. Zheng, W. Yang, K. Aldape, J. He, Z. Lu, *J. Biol. Chem.* **2013**, *288*, 31488.
[26] Q. Wei, O. Singh, C. Ekinci, J. Gill, M. Li, Y. Mamatjan, S. Karimi, S. Bunda, S. Mansouri, K. Aldape, G. Zadeh, *Acta Neuropathol Commun* **2021**, *9*, 67.
[27] a) K. Vigneswaran, N. H. Boyd, S. Y. Oh, S. Lallani, A. Boucher, S. G. Neill, J. J. Olson, R. D. Read, *Clin. Cancer Res.* **2021**, *27*, 1553; b) A. M. Barrette, H. Ronk, T. Joshi, Z. Mussa, M. Mehrotra, A. Bouras, G. Nudelman, J. G. Jesu Raj, D. Bozec, W. Lam, J. Houldsworth, R. Yong, E. Zaslavsky, C. G. Hadjipanayis, M. R. Birtwistle, N. M. Tsankova, *Neuro Oncol* **2022**, *24*, 694; c) C. Wei, X. Li, *Front. Pharmacol.* **2020**, *11*, 557429.
[28] a) A. Wimmer, S. K. Khaldoyanidi, M. Judex, N. Serobyan, R. G. Discipio, I. U. Schraufstatter, *Blood* **2006**, *108*, 3722; b) Y. T. Yeung, K. L. McDonald, T. Grewal, L. Munoz, *Br. J. Pharmacol.* **2013**, *168*, 591.
[29] S. M. Faisal, A. Comba, M. L. Varela, A. E. Argento, E. Brumley, C. AbelII, M. G. Castro, P. R. Lowenstein, *Front. Oncol.* **2022**, *12*, 1005069.
[30] a) K. Ravi, T. J. M. Manoharan, K.-C. Wang, B. Pockaj, M. Nikkhah, *Biomaterials* **2024**, *305*, 122428; b) M. Paolillo, S. Comincini, S. Schinelli, *Cancers (Basel)* **2021**, *13*, 2449.
[31] A. Pérez-López, A. I. Torres-Suárez, C. Martín-Sabroso, J. Aparicio-Blanco, *Adv. Drug Delivery Rev.* **2023**, *196*, 114816.
[32] S. Seo, S.-Y. Nah, K. Lee, N. Choi, H. N. Kim, *Adv. Funct. Mater.* **2022**, *32*, 2106860.
[33] J. P. Straehla, C. Hajal, H. C. Safford, G. S. Offeddu, N. Boehnke, T. G. Dacoba, J. Wyckoff, R. D. Kamm, P. T. Hammond, *Proc. Natl. Acad. Sci. USA* **2022**, *119*, 2118697119.
[34] a) C.-K. Shen, B.-R. Huang, W.-L. Yeh, C.-W. Chen, Y.-S. Liu, S.-W. Lai, W.-P. Tseng, D.-Y. Lu, C.-F. Tsai, *Eur. J. Pharmacol.* **2021**, *905*, 174216; b) Y. S. Liu, H. Y. Lin, S. W. Lai, C. Y. Huang, B. R. Huang, P. Y. Chen, K. C. Wei, D. Y. Lu, *Oncogene* **2017**, *36*, 5006.
[35] a) X. Wang, H. Wang, K. Jiang, Y. Zhang, C. Zhan, M. Ying, M. Zhang, L. Lu, R. Wang, S. Wang, D. J. Burgess, H. Wang, W. Lu, *J Control Release* **2019**, *293*, 201; b) X. Wang, N. Meng, S. Wang, L. Lu, H. Wang, C. Zhan, D. J. Burgess, W. Lu, *Mol Pharm* **2020**, *17*, 3281.
[36] a) Y. Zhang, Y. Wang, D. Zhou, K. Wang, X. Wang, X. Wang, Y. Jiang, M. Zhao, R. Yu, X. Zhou, *Oncogene* **2021**, *40*, 4580; b) M. Castellan, A. Guarnieri, A. Fujimura, F. Zanconato, G. Battilana, T. Panciera, H. L. Sladitschek, P. Contessotto, A. Citron, A. Grilli, O. Romano, S. Bicciato, M. Fassan, E. Porcù, A. Rosato, M. Cordenonsi, S. Piccolo, *Nat Cancer* **2021**, *2*, 174; c) B. Pontes, F. A. Mendes, *Diseases* **2023**, *11*, 86.
[37] Z. Liu, P. P. Yee, Y. Wei, Z. Liu, Y. I. Kawasawa, W. Li, *J. Cell Sci.* **2019**, *132*, jcs225714.
[38] a) M. A. Jourdain, J. Eyer, *J. Controlled Release* **2024**, *376*, 732; b) J. Quinlan, C. Inglut, P. Srivastava, I. Rahman, J. Stabile, B. Gaitan, C. Arnau, K. Baumiller, A. Gaur, W. A. Chiou, B. Karim, N. Connolly, R. Robey, G. Woodworth, M. Gottesman, H. C. Huang, *Adv. Sci.* **2024**, *11*, 2302872; c) S. Jeising, G. Geerling, R. Guthoff, D. Hänggi, M. Sabel, M. Rapp, A.-C. Nickel, *Photodiagn. Photodyn. Ther.* **2022**, *40*, 103049; d) S. R. Shah, J. Kim, P. Schiapparelli, C. A. Vazquez-Ramos, J. C. Martinez-Gutierrez, A. Ruiz-Valls, K. Inman, J. G. Shamul, J. J. Green, A. Quinones-Hinojosa, *Mol Pharm* **2019**, *16*, 1433.
[39] a) M. G. Yonk, M. A. Lim, C. M. Thompson, M. S. Tora, Y. Lakhina, Y. Du, K. B. Hoang, A. M. Molinaro, N. M. Boulis, W. Hassaneen, K. Lei, *Pharmacol Res* **2024**, *208*, 107390; b) J. Qi, L. Zhang, Z. Ren, Y. Yuan, J. Yu, Y. Zhang, L. Gu, X. Wang, Y. Wang, H. Xu, R. Yu, X. Zhou, *J. Nanobiotechnol.* **2024**, *22*, 495.
[40] B. A. Orr, H. Bai, Y. Odia, D. Jain, R. A. Anders, C. G. Eberhart, *Journal of Neuropathology & Experimental Neurology* **2011**, *70*, 568.
[41] Y. Liu-Chittenden, B. Huang, J. S. Shim, Q. Chen, S. J. Lee, R. A. Anders, J. O. Liu, D. Pan, *Genes Dev.* **2012**, *26*, 1300.
[42] a) L. Chen, X. Jin, J. Ma, B. Xiang, X. Li, *Front Cell Dev Biol* **2023**, *11*, 1204033; b) Z. Pan, Y. Tian, C. Cao, G. Niu, *Mol. Cancer Res.* **2019**, *17*, 1777.
[43] Y. Liu, W. Wu, C. Cai, H. Zhang, H. Shen, Y. Han, *Signal Transduct Target Ther* **2023**, *8*, 160.
[44] A. Dobin, C. A. Davis, F. Schlesinger, J. Drenkow, C. Zaleski, S. Jha, P. Batut, M. Chaisson, T. R. Gingeras, *Bioinformatics* **2012**, *29*, 15.
[45] M. Pertea, G. M. Pertea, C. M. Antonescu, T.-C. Chang, J. T. Mendell, S. L. Salzberg, *Nat. Biotechnol.* **2015**, *33*, 290.
[46] M. I. Love, W. Huber, S. Anders, *Genome Biol.* **2014**, *15*, 550.
[47] G. Yu, *The Innovation* **2024**, *5*, 100722.